Towards real-time condition monitoring of a transition zone in a railway structure using fibre Bragg grating sensors.
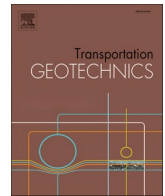
N.B. When citing this work, cite the original published paper.

(article starts on next page)

Towards real-time condition monitoring of a transition zone in a railway structure using fibre Bragg grating sensors

Kourosh Nasrollahi [a,*], Jelke Dijkstra [b], Jens C.O. Nielsen [a]

[a] Department of Mechanics and Maritime Sciences, Division of Dynamics/CHARMEC, Chalmers University of Technology, SE-412 96 Gothenburg, Sweden
[b] Department of Architecture and Civil Engineering, Chalmers University of Technology, SE-412 96 Gothenburg, Sweden

ARTICLE INFO

ABSTRACT

Differential settlement of ballast and subgrade is a common issue in ballasted railway tracks. In transition zones between two different track forms, such as between a ballasted track and a slab track, a dip in longitudinal level often develops on the ballasted side. To ensure the safety of railway operation and reduce maintenance and life cycle costs, it is necessary to monitor the condition of the transition zone in an economical manner and to detect any operational change at an early stage. In recent years with the advancement of fibre-optic technology, fibre Bragg grating (FBG) sensors have been more commonly applied in condition monitoring of railways due to their high precision and high acquisition rates. In this study, an FBG-based setup for in-situ long-term condition monitoring of track bed degradation in a transition zone has been developed and implemented to provide data for verification and calibration of a simulation model. The system is designed for measurements in an operational railway track in harsh conditions in the north of Sweden. The instrumentation along the transition includes four clusters, each with an optical strain gauge array on the rail web in one sleeper bay, and an accelerometer and a displacement transducer on the sleeper. It is shown that the implemented displacement and strain sensors are able to effectively capture the overall dynamic range of the system, indicating that the collected data can accurately represent the dynamic response of the transition zone in the short term and long term and be applied for the calibration of a simulation model.

Introduction

In a transition zone between two different forms of railway track, there is a discontinuity in track structure leading to a gradient in track stiffness. Examples include transitions between different superstructures, e.g., ballasted track to slab track, and/or between different substructures, e.g., embankment to a bridge or tunnel structure. Differences in loading and support conditions at the interfaces between track superstructure and substructure on either side of the transition potentially leads to differential track settlement. Hence, an irregularity in longitudinal rail level may occur on the ballasted side due to degradation mechanisms in the substructure, such as densification of ballast and embankment material and/or consolidation of the subsoil. This results in an amplification of the dynamic traffic loading along the transition, accelerating the degradation process of the foundation and resulting in a further deterioration of vertical track geometry [1–9]. In [10], it was reported that more than 50% of the studied bridge transitions faced a dip in longitudinal level with an average length and depth of 5.2 m and 33

mm, respectively. This highlights the importance of properly designing and maintaining transition zones to ensure smooth and safe railway operations.

Traditional design of ballasted track assumes that all sleepers have similar support stiffness [11]. However, in-situ variations in support conditions including voided sleepers are common. This was studied in a field test that captured the relation between railseat load and sleeper displacement along a ballasted track [12]. Based on measurements on five adjacent sleepers, it was concluded that sleeper displacement varied significantly from one sleeper to the next. The load–deflection curve was highly non-linear for those sleepers with poor support conditions. Such variations in support system stiffness over longer lengths of track can have a significant influence on track performance [13,14]. The main mechanism for the degradation of ballast is the cyclic loading due to passing traffic [15]. Another contribution to increased settlement is voids below the sleepers originating from poor tamping during construction or maintenance leading to an uneven load distribution along the track [3,16,17]. Furthermore, aggregate degradation can be

impacted by climatic factors, such as freeze–thaw cycles [18]. During a freeze–thaw cycle, entrapped water in ballast expands and contracts due to differing volume changes compared to the aggregate, leading to further particle breakage and settlement or heave.

The influence of an abrupt change in vertical stiffness at rail level on accumulated track degradation in a transition zone has been studied extensively using both field measurements and numerical simulations, see for example [1,6,7]. Traditionally, the aim of transition zone design has involved minimising the difference in track stiffness at rail level between the ballasted track and the engineering structure [7,19]. Mitigation measures to obtain a more gradual change of track stiffness include the implementation of under sleeper pads (USP), auxiliary rails and wider sleepers on the ballasted side, see [1,9,19]. These techniques help to distribute the loading on the foundation and reduce the risk of track degradation.

Many different types of sensor technologies have been employed to measure low-frequency vibrations and the performance of railway track in transition zones. This includes uniaxial and triaxial accelerometers, strain gauges, contact pressure cells, settlement pegs, video gauge systems (VGS), position sensitive detectors (PSD), multi-depth deflectometers (MDD) installed in the track bed, geophones, inclinometers, and linear variable displacement transducers (LVDTs), as well as remote sensing techniques such as interferometric synthetic aperture radar (InSAR), see [2,3,9,20–27]. For example, vertical track stiffness at rail level along a transition has been measured with accelerometers and using hydraulic actuators that apply harmonic loads on a wheelset [3,9,21]. Wang et al. [2,17] used a method based on InSAR for condition monitoring of a transition zone with bi-/tri-weekly data updates and millimetre-level precision. As a complement, an optical method based on digital image correlation (DIC) and a track geometry car were used to measure the settlement along the transition zone. Mishra et al. [28] employed five LVDTs to monitor the differential settlement generated in the ballast, sub-ballast, and subgrade layers in a transition zone. Coelho et al. [27] monitored a transition zone with reinforced concrete approach slabs linking the normal track onto a concrete culvert. In their study, accelerations and velocities of the track, soil, and approach slabs were measured. In addition, track settlement and pore water pressure were monitored over a one-year period.

Most of the systems mentioned above are (wired) electrical systems that involve installing (usually) cabled sensors on the track superstructure or within the track bed. Some systems use battery powered sensors that might drain at different times depending on the activity being recorded. This might create a potentially costly, never-ending battery maintenance program with different sensors being offline at different times and requiring manual maintenance [29]. This means trackside monitoring studies have generally focused on localised track sections, often for analysis of a particular property. Measurements over longer lengths of track to understand the variability of a certain track parameter are less common but have occasionally been implemented [9,13,14]. The main reason for the limited number of these studies originates from the technical, economical, and operational challenges that come with instrumenting long sections of track with the required spatial and temporal resolution of the physical quantity of interest.

An alternative approach is to use a system based on optical fibres. These types of systems fall into two categories: fibre Bragg grating (FBG) technologies, which are sensors inscribed into an optical fibre, and distributed optical fibre solutions where the optical fibre itself is used as a continuous sensor to provide distributed strain and temperature measurements along the entire fibre. Generally, compared to distributed optical sensing solutions, FBGs measure fewer points at higher precision and higher acquisition rates [30]. The most important features for railway applications are their immunity to electromagnetic interference (EMI) and the capability to multiplex many sensors and sensor types along a single fibre (including the possibility of using the two fibre ends to interrogate all sensors). This allows for simplifying the installations greatly, reducing cost, sensing over long distances and inherent self-

calibration capability. Strain information is encoded in the FBG reflection wavelength, which is an absolute parameter and thus the measurement value does not depend directly on the intensity fluctuations of the optical source or the losses between the FBGs and the interrogation unit. Furthermore, FBG sensors can be interrogated at very high frequencies, which is important for detecting dynamic events such as vibrations from wheel–rail impact.

Optical sensors have been used in railway condition monitoring, for example for axle counting, derailment detection, train wheel condition monitoring, train vibration, weight measurements, and for structural analysis of railway track in general, see refs. [26,31–34]. For instance, Wang et al. [35] attached two FBG strain sensors on the rail web as a bi-directional device to measure the longitudinal force in a continuously welded rail (CWR) in a high-speed railway line. Wheeler et al. [22,25,26] measured rail strains using Rayleigh backscattered, distributed optical fibre sensors. Their field test instrumentation included a 7.5 m long section of rail with nylon-coated single-mode fibres installed on the rail web at 20 mm and 155 mm from the bottom of the rail, respectively. The measured rail strains were used to determine shear force, which was used with the known static wheel loads as part of the calibration to determine the rail seat load for 14 consecutive sleepers as the train passed over the instrumented track. These data were then combined with measurements of dynamic rail displacement captured using DIC to process the rail seat load–deflection relationships for each sleeper. In contrast to FBG solutions, more sleepers could be monitored simultaneously at the expense of lower acquisition rates (hence the train speeds were very modest).

This study aims to demonstrate an FBG-based setup for condition monitoring of track degradation in a transition zone of an operational railway line, in terms of sleeper displacements and settlements over a long period of time. The instrumentation setup incorporates an optical interrogator and four sensor clusters along the transition, each consisting of a displacement transducer, an accelerometer, and a strain array. For practical deployment in harsh conditions in a railway section that is poorly accessible, robustness and cost were considered in addition to the precision and acquisition rates required. The sensor setup has been validated and calibrated in quasi-static conditions using the known axle loads of a slowly moving vehicle.

Test site description

The test site is located on the Swedish heavy haul line *Malmbanan* in a passing siding at *Gransjö*, with coordinates of latitude 66.064 and longitude 21.407, see Fig. 1(a). Malmbanan is a single-track railway line in the northern part of Sweden. The traffic conditions at the test site allow recording of approximately 45 train passes per day. Traffic is dominated by iron ore freight trains with axle loads up to 32.5 tonnes operating from the mines in *Kiruna* and *Malmberget* to the ports in *Narvik* (in Norway) and *Luleå*, see Fig. 1(b). The bottom dumper wagons are supported and guided by three-piece bogies, see Fig. 2(a). The speed of the loaded heavy haul trains is 60 km/h (70 km/h in tare conditions). In addition to the iron ore trains, traffic consists of passenger trains at maximum speed 135 km/h and other types of freight trains. Based on a wheel impact load detector located at *Sunderbyn*, 50 km from the test site, the annual traffic load is in the order of 15 MGT (Mega Gross Tonnes) including about 850 000 axles in (loaded and unloaded) iron ore trains [36], see Fig. 2(b). The estimated traffic load distribution at Gransjö is displayed in Fig. 2(c). Further information about the traffic load is provided in Table 1.

The instrumented track section represents a transition between conventional ballasted track and a 48 m field demonstrator section of a Moulded Modular Multi-Blocks (3MB) slab track, see Fig. 1(a). The 3MB concept is a reinforced standard precast slab track designed for both mixed traffic and high-speed traffic [37]. The rail in the slab track section is discretely supported at fixed rail seat distance 0.6 m. The 3MB track is based on 4.8 m long modules. Each module comprises a base slab
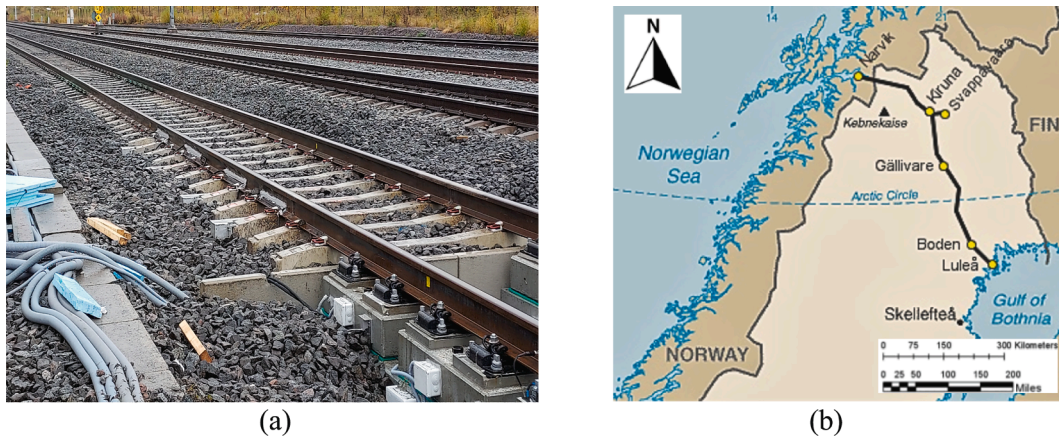
Fig. 1. (a) An overview of the transition zone between ballasted track and 3MB slab track at Gransjö, north of Boden, Sweden. The direction of traffic for loaded iron ore trains is moving from the ballasted track to the slab track. (b) Geographical location of the iron ore line Malmbanan.
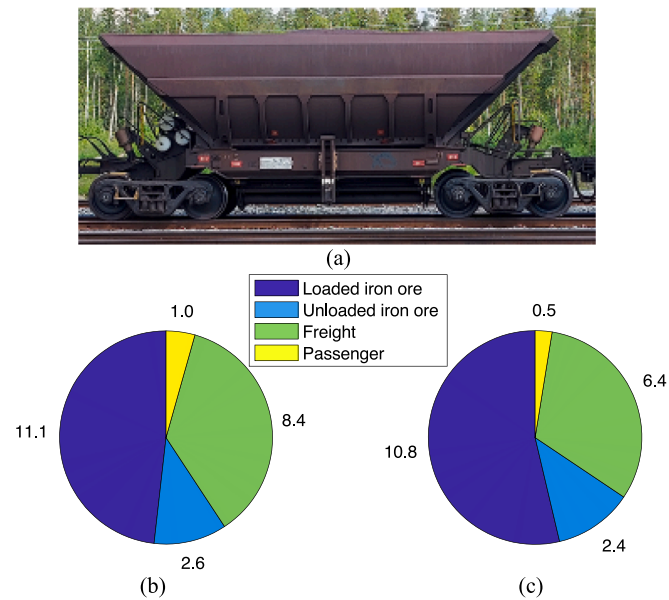

Fig. 2. (a) Iron ore wagon consisting of a car body and two bogies, each consisting of two wheelsets. Accumulated traffic load [MGT] at (b) Sunderbyn wheel impact load detector station and (c) Gransjö.

Table 1
Train and traffic data at test site Gransjö.

	Iron ore trains	Passenger trains	Freight trains
Speed range of loaded trains at Gransjö (km/h)	60	≤ 135	≤ 80
Speed range of unloaded trains at Gransjö (km/h)	70		≤ 80
Average total train length (m)	750		Varying
Axle load of locomotive (tonnes)	29.5	17	
Maximum axle load of wagons (tonnes)	32.5		25
Axle load of tare wagons (tonnes)	5		Varying
Wheelset distance in locomotive bogie (m)	1.92		
Distance between bogie centra in locomotive (m)	12.8		Varying
Nominal distance between bogie centra in two adjacent wagons (m)	3.52		
Bogie wheelbase in a wagon (m)	1.78		Varying
Distance between bogie centra in coach/wagon (m)	6.77		Varying
Number of axles per locomotive	6	4	4
Number of axles per wagon	4	4	2 or 4
Accumulated traffic load at Gransjö (MGT/year)	13.5	0.5	6.4
Number of wagons per train	68	Varying	Varying

consisting of two longitudinal reinforced concrete beams that are connected by two transverse beams, and eight precast moulded concrete blocks, four on each longitudinal beam of the base slab. Elastomeric strips at the interfaces between base slab and blocks provide vibration isolation and prevent hammering of the moulded blocks against the base slab [36]. The 3MB track at Gransjö was constructed in September 11–15, 2022, as a part of the Horizon 2020 Shift2Rail EU project In2Track3. It was decommissioned in August 2023.

The ballasted track includes 60 kg/m rails, rail fastenings with 10 mm rubber rail pads, concrete sleepers designed for axle load 35 tonnes, and nominal sleeper distance 0.6 m. In addition, under sleeper pads were implemented along 15 m (25 sleepers) of the ballasted track to reduce the stiffness gradient in the transition. The extreme weather conditions with temperatures down to −40 °C in the winter and relatively warm summers lead to recurrent issues with freeze–thaw conditions and evolving irregularities in track geometry. Thus, the implementation of a non–frost-susceptible track structure is required down to a certain depth depending on the frozen depth layers. Since the site location is based on an old track design, the frost insulation was installed at the depth of 1 m, while for the new slab track frost insulation

boards were installed underneath the sub-ballast layer. In general, the settlement rate along Malmbanan varies significantly depending on the local conditions and properties of the subgrade [38].

The subgrade at the site consists almost exclusively of moraine, mixed with big blocks [39] with a maximum depth of 5 m to bedrock. The embankment height varies between 2 and 2.5 m. Due to years of maintenance involving tamping and re–ballasting of the track, the thickness (nominally 30 cm) of the ballast layer has reached 80 cm. During the construction of the 3MB slab track, an extra excavation depth was required to remove the big blocks. The excavated volume was replaced with not sufficiently compacted back fill material before construction of the slab, which led to significant settlement of the slab track soon after construction. The infrastructure was stabilised by the passing of trains at reduced speed until 0.1 MGT of accumulated traffic. Subsequently, the quality of the track geometry was controlled with a track geometry recording car before allowing nominal train speeds. Due to the excessive settlement of the slab track soon after construction, the fasteners on the slab side were adjusted to their desired height by sliding shims after 20 days of operation. At the same time, the first six sleepers on the ballasted side were tamped to restore the longitudinal level.

To determine the stiffness and stratification of the layered substructure at the test site, a multi-channel analysis of surface waves

(MASW) measurement was performed. In the MASW survey [39], the dispersion of Rayleigh waves on the ground surface acquired using vertical geophones was used for further interpretation of the small strain shear stiffness following the original method proposed in [40]. Young's moduli were determined based on measured shear wave velocities, and by assuming typical values for Poisson's ratio and density according to relevant literature, see [36,39,41]. A summary of the measured and derived soil properties is provided in Table 2.

Monitoring setup

A setup for condition monitoring was developed and implemented to assess the influence of traffic load on the accumulated differential settlement in the transition zone. Condition monitoring of the transition zone commenced immediately after the track construction on the 15th of September 2022. These continuous measurements enabled the quantification of evolving changes in the transition zone in terms of rail bending moment and permanent sleeper displacement. Another aim of the field test at Gransjö is to verify and calibrate the numerical model for prediction of long-term differential settlement in a transition zone presented in [36]. However, the calibration and validation of the model are not within the scope of this paper.

Pre-test simulations

Prior to the instrumentation, advanced numerical analyses were performed to select the requirements for the monitoring system, i.e., where and what to measure and at which sampling rate. A vehicle model of one iron ore wagon and a two-dimensional (2D) finite element model of the track were used to predict the vertical dynamic vehicle–track interaction in the transition zone between the ballasted track and the 3MB slab track. The simulation model implemented in MATLAB is presented in Fig. 3. The 2D model was used to calculate vertical wheel–rail contact forces, rail and sleeper vibrations (displacements, velocities, and accelerations) and loads on sleepers (rail seat loads and loads acting at the interface with the ballast). The simulation model is described in detail in [36,42].

The procedure for simulation of long-term degradation in the transition zone is based on an iterative approach, where the time-domain model of dynamic vehicle–track interaction in the short-term is integrated with a model for accumulated substructure settlement in the long-term. The calculated load maxima at each interface between sleeper and ballast in the ballasted track section, generated by the combination of gravity load and the load induced by each of the wheels of the vehicle model, are used as input to a settlement model. The model of the track dynamics is updated in each iteration step to account for the new states of the sleeper support conditions. By taking several iteration steps, the accumulated (long-term) differential settlement and redistribution of foundation loads between adjacent sleepers are determined [36]. In the pre-test simulations, the settlement below the slab track was neglected relative to the settlement in the ballasted track section. This is because the contact pressure between base slab and foundation was expected to be significantly lower than the corresponding contact pressure at each sleeper.

The model results for the virgin transition zone (without a dip in the ballasted track section due to differential settlement) indicated

maximum wheel–rail contact forces in the order of 147 + 5 kN, where the 147 kN is the static wheel load and 5 kN is the magnitude of the dynamic load induced by the stiffness gradient. Furthermore, maximum sleeper displacement upon a single axle passage was in the order of 1–2 mm with 0.1 mm precision, while sleeper acceleration maxima was 4–5 g [36]. Based on Refs. [26,36,42], the axial strains in the rail web were in the range of 200–300 με. Accordingly, maximum rail bending moment was in the order of 25 kNm. As expected, the simulated accumulated settlement after three years of traffic for the sleepers near the transition was higher than elsewhere (leading to a dip in longitudinal level) and predicted to be in the order of 3–10 mm.

Instrumentation

The instrumentation plan included sensors for the measurement of i) axial rail strains to assess rail bending moment and rail seat load; ii) vertical sleeper displacement; iii) vertical acceleration at sleeper end. An overview of the positioning of the sensors is shown in Fig. 4. The setup includes four permanent clusters placed at sections between two sleepers in sleeper bays 3, 5, 8, and 11 numbered from the transition. Each FBG-based cluster consists of one accelerometer, one displacement transducer, and one strain array including four strain gauges. One extra accelerometer was placed on a sleeper in the ballasted track far from the transition and another one on the first block on the slab track side. Four temporary electrical strain gauge bridges were added to measure wheel–rail contact force. The permanent installation of sensor clusters was used for condition monitoring of the transition, whereas the temporary installation was used to monitor dynamic wheel–rail contact forces for a single train. In total, 30 FBG sensors were installed. Aluminium covers and cable conduits were added to protect the sensors and cables respectively from mechanical damage and the harsh weather conditions.

Given the sensor requirements, harsh site conditions, operational railway track and budget constraints, FBG sensors were selected for all positions except for the shear force measurements in the rail web. Furthermore, using FBG sensors greatly reduced the installation time which was required to meet the narrow installation window during the construction of the 3MB slab track. Another benefit was the simplified routing of optical cables so that the interrogator (Optics11 I4G optical) could be placed in a heated cabinet to keep the logger within operational temperatures (0–60 °C), as well as near the available power source and data connection provided by the track owner. Other equipment at the site was a field computer, an additional hard drive, a junction box, two temperature sensors (inside and outside of the cabin), a thermostat, a fan, a 4G antenna to provide a backup data connection, and a network switch. The interrogator continuously measured all sensors at the pre-set fixed sampling frequency of 2 kHz and distributed the data on a network socket that was connected to the computer. A custom LabVIEW based programme FemtoGateway read, formatted, and stored the data locally. Subsequently, the data was synchronised with a server at Chalmers University of Technology. Here, the ability for remote configuration of the system helped to adapt to the needs of the project.

The sampling frequency $f_s = 2$ kHz allowed for the combination of (slowly evolving) static and dynamic measurements of the Bragg wavelength by using add/drop wavelength-division multiplexing. It also allowed for the measurement of all sensors connected in series on each

Table 2
Properties of substructure layers at Gransjö evaluated from measured shear wave velocities. From [39].

Layer	Layer number(q)	Layer depth H (m)	Density ρ (kg/m^3)	Poisson's ratio ν	Shear wave velocity V_s (m/s)	Elasticity modulus[1] E (MPa)
Ballast	1	0.3	1800	0.2	125	67.5
Sub-ballast	2	1	2100	0.3	175	161.7
Subgrade layer 1	3	2	2100	0.25	300	472.5
Subgrade layer 2	4	8	2100	0.25	> 400	> 800

[1] Young's modulus: $E = 2\rho\, V_s^2(1 + \nu)$.
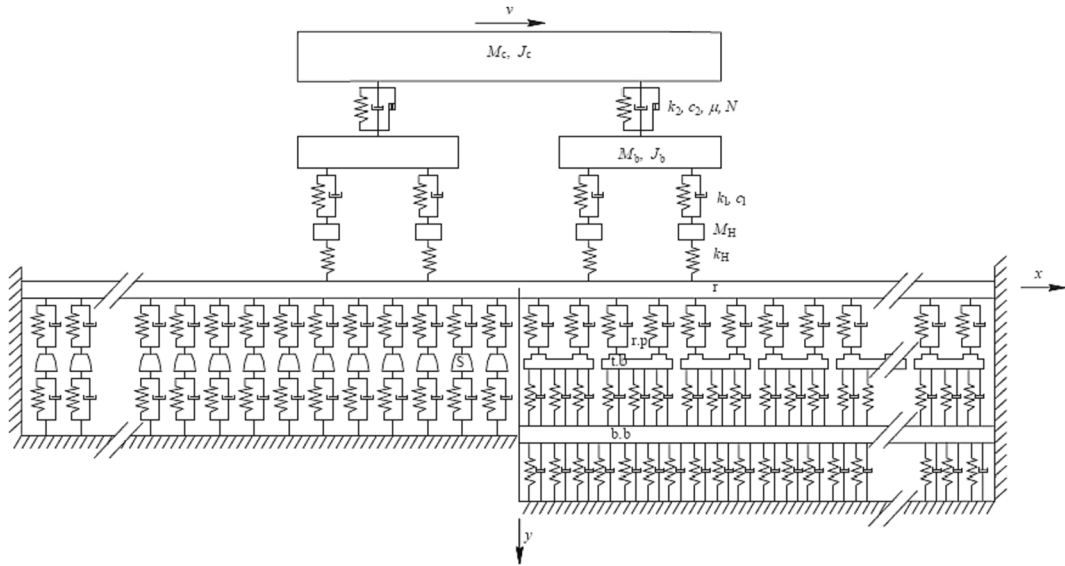
Fig. 3. Principle sketch of vehicle and track models ($x < 0$: ballasted track, $x > 0$: slab track). The track model contains rail (r), top block (t.b) and base slab or base block (b.b) modelled by Euler-Bernoulli beam elements. The base slab is supported by a Winkler foundation. The sleepers (s) are rigid masses supported by a spring-damper connection (representing the ballast/subgrade) with piecewise linear stiffness properties. The sleepers selected for long-term measurements are sleepers 3, 5, 8, and 11 numbered from the transition [36].
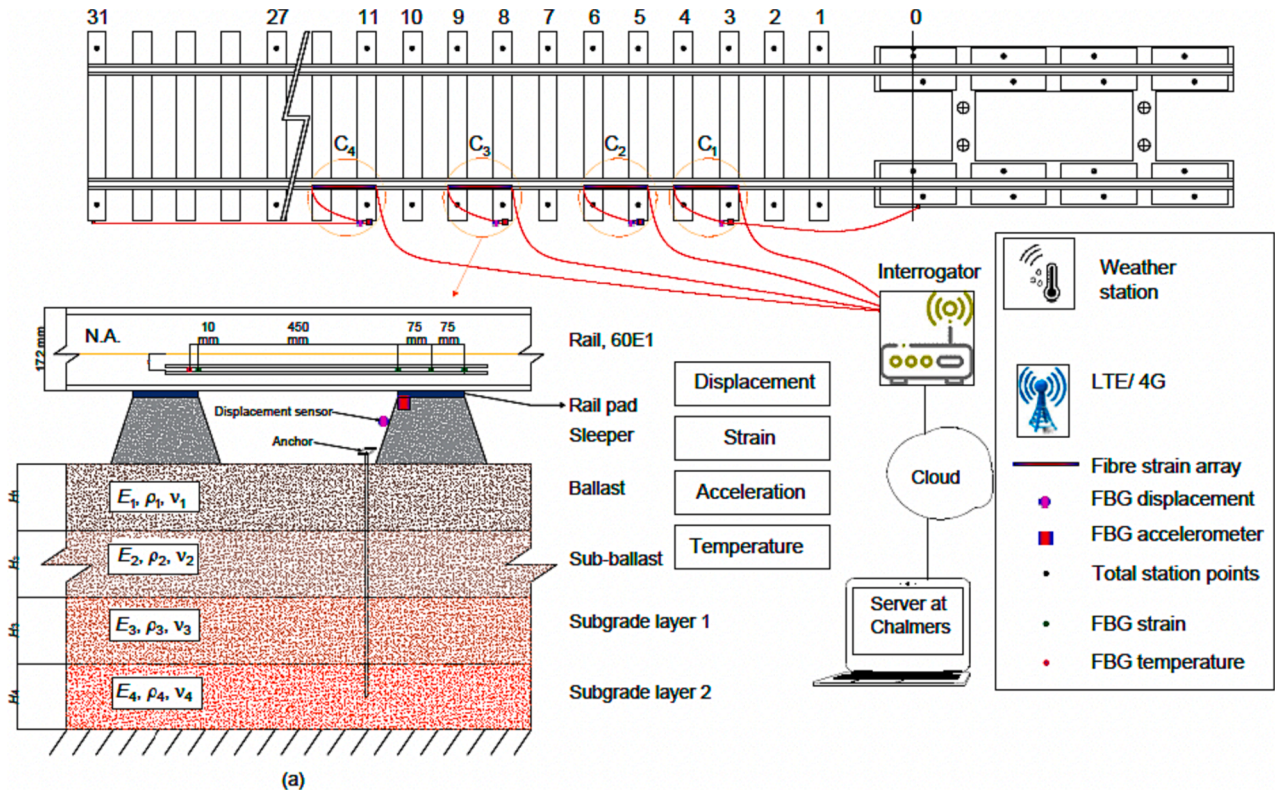

Fig. 4. Schematic representation of the data acquisition system in the transition zone between ballasted track and 3MB slab track. The setup consists of four clusters (C1–C4) each including a strain array (four strains on the rail web), a sleeper displacement transducer, and an accelerometer on the sleeper end.

channel, operating within predefined wavelength bands. The sampling frequency was sufficiently high to capture the quasi-static rail bending for the train loads and speeds in this trial as well as to reduce noise in the subsequent signal processing steps [43].

In this study, the conventional Bragg grating strain and temperature sensors were used to measure axial strain and temperature along the rail, respectively. The bandwidth of each strain sensor was such that it could

measure a wavelength shift of the Bragg resonance as large as ± 1.25 nm, which corresponds to an axial strain of ± 1250 $\mu\varepsilon$, see Table 3. This span is sufficiently large for railway monitoring. The sensitivity of the FBG sensor is expressed in [pm/$\mu\varepsilon$]. Each strain array was welded at 31 mm below the neutral axis on one side of the rail to measure the magnitude of axial strain due to rail bending, see Figs. 4 and 5. The rail surface was polished and dried before the installation. Strain sensors 1, 2 and 3 in

Table 3

Sensor specifications.

Technical parameter	Specifications		
	FBG-based strain sensors	Accelerometer	Displacement
Operating temperature	– 20 to 60 °C	– 40 to 60 °C	– 30 to 30 °C
Measuring range	± 1500 με	± 150 g	0–50 mm
Resolution	1 με	10 nm/g	30 μm

each cluster were placed above the same sleeper, while sensor 4 was located near the adjacent sleeper, see Fig. 5.

A high-precision distance-measurement system is necessary to monitor the vertical movement of the sleepers. Therefore, the vertical displacement of four sleepers (3, 5, 8, and 11) were assessed using FBG-based displacement transducers installed at the sleeper ends. The displacement of each sleeper was measured with respect to a fixed anchor embedded deep in the ground (fixed reference). The depths of the anchors were in the order of 2, 2, 0.5, and 4 m for sleepers 3, 5, 8, and 11, respectively. Due to its size and the limited available space, the displacement transducer was positioned horizontally in parallel with the sleeper. Using an L-shaped mechanism rigidly connected to the sleeper end, the vertical displacement of the sleeper is converted to horizontal tension/compression of the displacement transducer. As the sleeper moves downwards, the descent of the horizontal leg of the L-shaped mechanism corresponds to a horizontal displacement of the vertical leg. Based on the corresponding elongation of the displacement transducer, the vertical displacement of the sleeper relative to the anchor is measured. The displacement transducers were adjusted on site on 2022-10-04, 2022-10-25 and 2023-01-27 to ensure that the measured displacements fell within the measurement range (hence FBG wavelength bandwidth). Fig. 6 shows a general view of the positions of the mechanism, the displacement transducer, and the accelerometer.

Further, vertical accelerations were measured using six FBG-based accelerometers. Five of these were placed at sleeper ends 3, 5, 8, 11, and 31, while one was positioned on the first block on the slab track side.

Wheel–rail contact force is a primary indicator of the dynamic vehicle–track interaction. In the current setup, contact forces were considered complimentary to the condition monitoring setup with the FBG sensors. Using a standard setup, shear deformations of the rail were measured on October 25th, 2022, and May 17th, 2023, in sleeper bays 3, 5, 8, and 11 numbered from the slab track. A half-bridge containing two waterproof strain gauges, each with a sensing area of 6 mm × 2.2 mm, was glued on the neutral axis of the rail within a given span between two adjacent sleepers, and oriented at ±45° with respect to the horizontal and vertical coordinate axes. Two extra half bridges were glued to the other side of the rail in sleeper bay number 3 to study any effects of lateral offset in the wheel load. A data logger fitted with full-bridge completion modules was used to sample the strain gauges at 10 kHz.

Data processing

When the rail is subjected to bending due to a passing vehicle, any change in axial strain and temperature is measured using the FBG-based strain gauges that were mounted on the rail web. A change in strain is recorded as a change in length of the fibre, which causes a (frequency) shift in the optical spectrum. In the applied setup, strain and temperature were recorded in independent gratings. However, during a single train passage the temperature variation is negligible. Strain signals were high-pass filtered at 1 Hz using a high-pass filter (a phase-preserving FIR filter) in MATLAB to adjust the baseline of the signal and prevent low-frequency drift.

Each wheel in the passing train is characterised by a peak in the measured time history of the strain signal. For a given bogie wheelbase s, train speed v was determined by evaluating the separation in time Δt between two strain maxima

$$v = \frac{s}{\Delta t} \tag{1}$$

The type of train was determined by evaluating the total number of peaks in the signal using the *findpeaks* function in MATLAB. Assuming
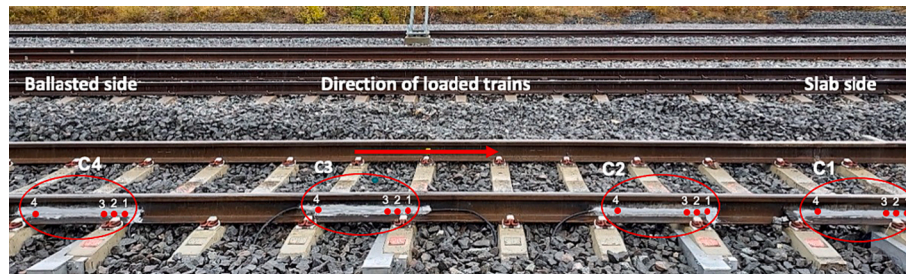

Fig. 5. An overview of the four clusters (C1–C4) and the strain sensor numbering for each cluster.
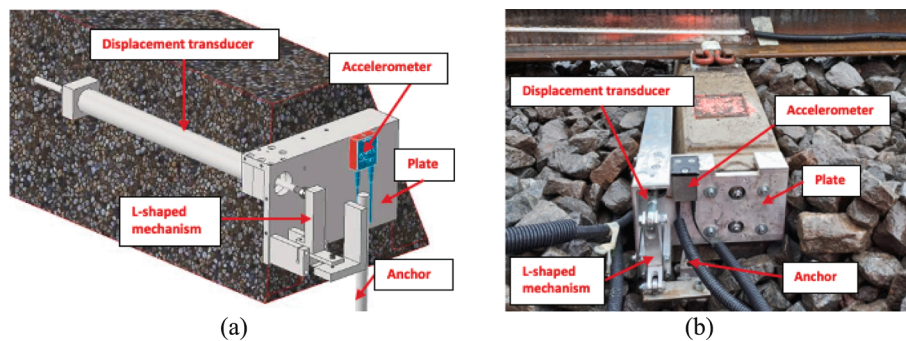

Fig. 6. Detail of instrumented sleeper containing a vertical base plate, an L-shaped mechanism, one accelerometer and one displacement transducer. (a) The designed setup. (b) Overview of an instrumented sleeper with an accelerometer and a displacement transducer. The positions of the anchor tip and the L-shaped mechanism are shown.

Euler-Bernoulli beam theory is valid, the measured axial strain ε at distance y from the neutral axis of the rail is used to determine the curvature κ of the rail as

$$\kappa(x) = \frac{\varepsilon(x)}{y} = \frac{d^2 w(x)}{dx^2} \qquad (2)$$

Here $w(x)$ is the vertical rail deflection at longitudinal coordinate x. For a known rail cross-section with bending stiffness EI, the rail bending moment $M(x)$ along the rail is determined as

$$M(x) = EI \bullet \kappa(x) \qquad (3)$$

Based on the bending moment evaluated at each time instant for the three positions on top of a sleeper, a second-order polynomial (using "polyfit" in MATLAB) can be evaluated to approximate the bending moment distribution $M(x)$ across the width of the sleeper

$$M(x) = w_0 + w_1 x + w_2 x^2 \qquad (4)$$

The distribution of shear force in the rail is determined by

$$T(x) = \frac{dM(x)}{dx} \qquad (5)$$

In theory, the time history of the railseat load could be determined by evaluating the time-variant difference in shear force across the width of the rail pad (but not while a wheel is within the instrumented section since then there are two unknown loads). However, this has not been considered in the present study.

The displacement transducers were found to be sufficiently fast to also record the transient response of the sleeper end displacement. The displacement signal was filtered such that the signal contains a stationary region in which there is a regular and repeating signature of sleeper displacement from the vehicles in a train passage, but without filtering out relevant information around the vehicle passing frequency. In this study, a 4th-order low-pass Butterworth filter with corner frequency of 30 Hz was applied to remove the contributions at frequencies above those that were dominating the track bed movement. While the frequencies of interest may be within a relatively narrow range (1–30 Hz), data must be acquired at much greater logging rates to aid processing and eliminate noise and aliasing (in this study 2 kHz) [43]. The zero-phase digital filtering *filtfilt* was applied to preserve the phase of the signal.

The recorded acceleration signals were high-pass filtered at cut-off frequency 1 Hz based on recommendation from the provider of the sensor. The cut-off frequency can also be selected based on the signal-to-noise ratio [44]. Unfortunately, it was found that the signal-to-noise ratio in the measured acceleration was too low to obtain reasonable data for sleeper displacement reconstruction.

Time histories of wheel–rail contact force $F_{w/r}(t)$ were evaluated based on measurements with the shear strain bridges. Data was recorded using a separate data acquisition (DAQ) system with a sampling rate of 10 kHz. A slowly passing locomotive (5 km/h) with known axle loads (locomotive weight 90 tonnes) was used to calibrate and verify the complete instrumentation setup on site. This static calibration was subsequently used for conversion of the dynamic signals that are expected to be up to 10% higher, yet the dynamic response is still within the linear range of the measurement system. The calibration was conducted on May 16th–17th, 2023.

Demonstration of the monitoring setup

To demonstrate the robustness of the monitoring setup, rail strain and sleeper displacement have been continuously measured using the set of FBG sensors and an interrogator with high acquisition rate (2 kHz or more). For each given train passage, the train speed, number of axle passings, vehicle type, and the short-term dynamic response of sleeper displacement and rail bending moment have been assessed. Further,

based on continuous measurement over many train passages, the long-term evolution of sleeper displacement and settlement have been investigated.

The time history of a measured Bragg wavelength shift signal for a complete iron ore train passage is shown in Fig. 7(a). The number of axles is obtained by counting the total number of peaks in the strain signal using the *findpeaks* function in MATLAB. This particular signal can be identified to correspond to an iron ore train with 284 axles, where the first 12 axles originate from the two CoCo locomotives at the front of the train, while the following 272 axles are due to the four wheels in each of the 68 loaded wagons. Each individual wheel passing is clearly detectable. Next, the Bragg wavelength shift signal has been converted to the corresponding rail strain signal and filtered using the previously described high-pass filter with cut-off frequency 1 Hz. A section of the resulting strain signal corresponding to the passage of three iron ore wagons (the passage of one bogie from each of the two adjacent iron ore wagons are also shown as the first two and last two peaks in the signal) is shown in Fig. 7(b). The minimum induced strain due to a wheel passing on the track generates more than 150 pm wavelength shift (peak to peak), and the noise in the determination of the Bragg wavelength is less than 10 pm. The train speed is determined by the measured time between two strain maxima and the known bogie wheelbase. In this example, it was found that train speed varied in the range 56–59 km/h. The signal recorded with the temperature sensor (not shown here) indicated a very slowly changing ambient temperature. Nevertheless, this variation was considered for correcting the baseline change in strain.

Due to the periodic passing of iron ore wagons, certain frequencies are dominating the signal. These frequencies are determined by the speed and the configuration of the train with car body spacing $L_c = 10.3$ m [34]. Considering the variation in train speed, see above, the corresponding fundamental car body passing frequency is in the interval $f_c = v/L_c = 1.5$–1.6 Hz. The passing frequency and higher-order harmonics can be observed in the Fourier transform of the measured strain signal, see Fig. 8.

Rail bending moment

For a given train passage and for each of the four clusters, examples of rail bending moments evaluated using Eq. (3) are shown in Fig. 9. Each subfigure illustrates the rail bending moment in the three positions 1, 2 and 3 above one sleeper, cf. Fig. 5. Based on the maximum bending moment in position 2 generated by each of the axles in the train, the associated cumulative distribution functions are presented in Fig. 10. The variation in maximum rail bending moment per wheel passage is due to differences in axle load, vehicle configuration and interaction between adjacent wheels, and the dynamic wheel–rail interaction for example due to the presence of wheel out-of-roundness. It is observed that the order of magnitude of maximum rail bending moment at sleepers 5 and 8 is lower than at sleepers 3 and 11. Since rail bending moment is increasing with decreasing support stiffness, this can be used as an indication of that sleepers 3 and 11 are not as well supported as sleepers 5 and 8. Further, in Fig. 9, it is noted that the rail bending moment evaluated for sensor 1 in each of the clusters is consistently different from the bending moments evaluated for sensors 2 and 3. The reason for this effect is unknown. Unfortunately, this has the consequence that rail seat loads could not be evaluated with sufficient accuracy according to the procedure described in Section 3.3.

Sleeper displacement

During one load cycle (e.g., due to a passing wheel), the deformation of a given position in the track substructure contains an elastic (reversible, i.e., fully recoverable upon unloading) part and a plastic part that is irreversible. Accumulated over time, the permanent deformation is the so-called long-term degradation or settlement. An example of the
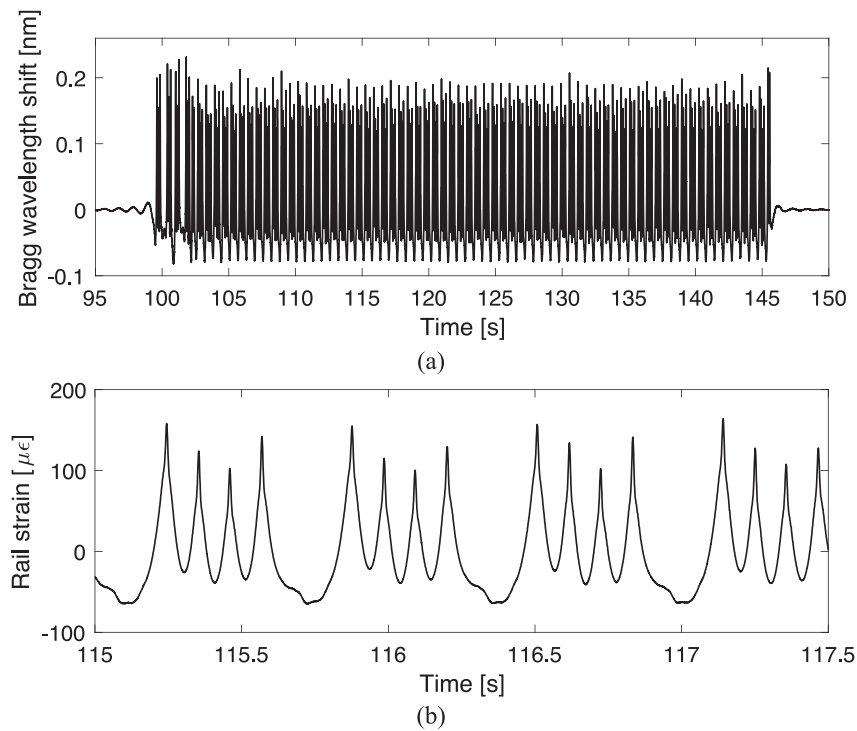
Fig. 7. Time history of high-pass (1 Hz) filtered signal. (a) Bragg wavelength shift for complete loaded iron ore train passage, (b) rail strain for part of the signal. Train speed $v = 56$–59 km/h. Measurement from 2022-12-07.
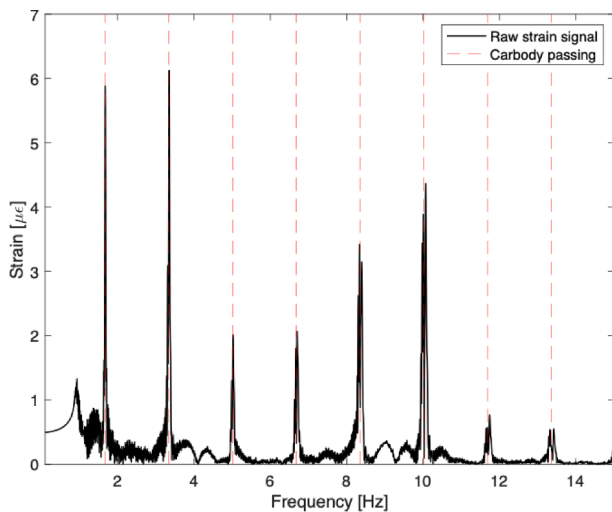

Fig. 8. FFT of raw strain signal. Fundamental car body passing frequency and higher-order harmonics. Measurement from 2022-12-07.

measured time history of the displacement of sleeper 5 is illustrated in Fig. 11. In this example, the displacement is presented relative to the displacement before the arrival of the first wheel in the first locomotive. The signal has been low-pass filtered with cut-off frequency 30 Hz (about three times the wheelset passing frequency). The offset in the displacement signal a few minutes after the passing of the last wheel in the trainset (when the track has been fully recovered) is considered as the increment in permanent sleeper displacement (settlement) generated by one iron ore train.

In the low-pass filtered signal in Fig. 11, it is observed that the wheels of the iron ore wagons cause a higher deflection than the first wheels of the locomotive even if the axle loads are similar. This is due a transient at the start of the sequence, which is an artefact from the processing of

the signal [45]. However, the shift in the signal associated with the at-rest positions before and after the train passage is tracked with high fidelity. The signature and amplitude of the sleeper displacement depend on the configuration and magnitude of the passing wheel loads. For example, it is observed that the track structure does not have the time to recover from the deflection caused by the preceding axles. As for the rail bending moment, there are variations between the displacements under each wheel because of differences in axle load, out-of-round wheels, etc. For long trains formed of several identical vehicles, and where filtering has been appropriately applied, the central portion of the data gives a repeating waveform that may be referred to as a stationary wave.

The low-pass filtered displacements for sleepers 3, 5, 8 and 11 due to the passing of three pairs of adjacent bogies in adjacent wagons in the stationary part of the signal are compared in Fig. 12. For each sleeper, the displacement is presented relative to the displacement level before the first axle in the first locomotive. Note that each individual wheel passage is not visible in the signal. Instead, each plateau of maximum level (positive sleeper displacement is downwards) corresponds to the passing of four wheels from two adjacent bogies in two adjacent wagons. In between each set of four wheels, there is sufficient time for a partial upward recovery of the sleeper since the distance between the two bogies in an iron ore wagon is longer than the bogie wheelbase, see Fig. 2 (a). The results indicate a tendency to larger displacement magnitudes towards the 3MB slab track, with substantially higher displacement maxima (in the order of 7 mm) for sleeper 3. This shows that sleeper 3, which is closest to the transition, is poorly supported and probably voided.

Fig. 13 confirms that sleeper 3 has the cumulative distribution with the largest peak displacements. Note that these are the total displacements, incorporating both the reversible and irreversible parts of sleeper displacement. For sleepers 3, 5 and 8, these findings corroborate well with the measured cumulative distributions of maximum rail bending moment (Fig. 10), illustrating that poor (low stiffness) track support leads to both higher rail bending moment and higher sleeper displacement. Consequently, sleepers 5 and 8 have a better support, whereas sleepers 3 is poorly supported. For sleeper 11, the level of displacement
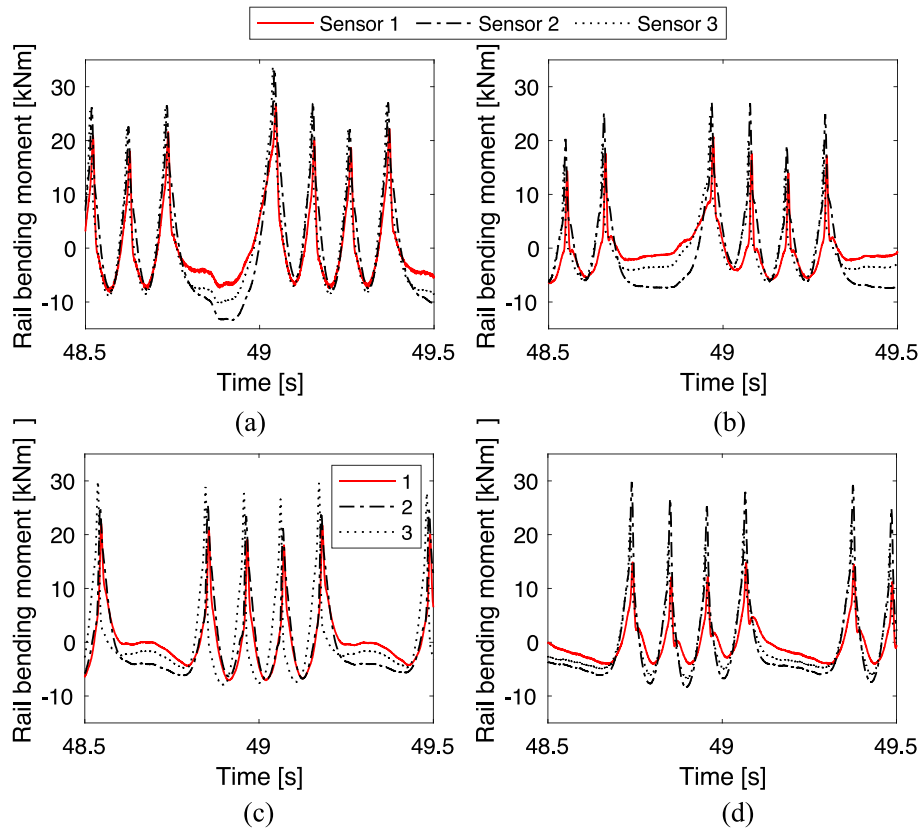
Fig. 9. Rail bending moment above four sleepers along the transition. (a) Sleeper 3, (b) sleeper 5, (c) sleeper 8, (d) sleeper 11. The loaded trains first pass over sensor 3, and then 2 and 1. Measurement from 2022-12-07.
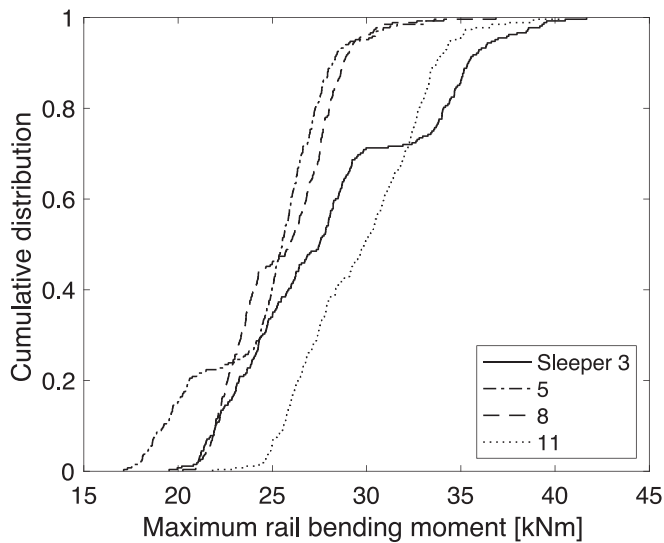

Fig. 10. Cumulative distributions of maximum rail bending moment along the transition zone due to the passing of one loaded iron ore train. Measurement from 2022-12-07.

is low while the magnitude of the rail bending moment is high. The reason for this is unknown.

A more direct result of the long-term evolution of sleeper settlement is shown in Fig. 14(a,b). Here, data has been extracted from times between train passages. The accumulated traffic load is indicated by the dashed vertical lines, where the distance between each pair of lines represents 1 MGT of traffic load. For all sleepers, it is observed that the high settlement rate directly after the installation of the transition zone

slowed down after a few weeks of traffic. In particular, sleeper 8 seems to have stopped settling after the ballast layer had been compacted. This seems to be in line with that the anchor at sleeper 8 could only be drilled down to a depth of 0.5 m indicating a stiffer support (potentially due to a large block similar to those that were found during excavation for the slab track). As discussed above, tamping of the first six sleepers adjacent to the 3MB slab track was performed on October 4th (indicated by the vertical dash-dotted line in Fig. 14(a,b)). Since the tamping maintenance activity reduced the densification of the ballast (and did not add any new ballast), sleepers 3 and 5 were again subjected to high settlement rates that slowed down after a few weeks of traffic. The large oscillations in the long-term trend of settlement for sleeper 3 is unknown. However, based on the results in Figs. 11 and 12, it can be concluded that this sleeper is voided and subjected to severe vibrations and particularly difficult measurement conditions (Fig. 14).

Frost heave is a significant issue on Malmbanan. The ambient temperature at Gransjö is displayed in Fig. 14(c). The Swedish Transport Administration measures frost depth using frost sticks that measure the temperature at several levels down to a depth of a couple of metres to form a temperature profile. Frost depth recorded at a station near the test site is shown in Fig. 14(d). Before end of October, it is seen that the ground was not frozen at all. Until mid-December the ground started freezing gradually down to 2 m depth, and between mid-December 2022 to beginning of May 2023 more than 2 m of the ground was frozen [46]. When the ambient air temperature dropped below about −10℃ and the frost depth exceeded 2 m, it can be seen that the settlement of sleepers 5 and 11 seems to have stopped and instead the degradation curves are reversed towards smaller settlements. Thus, this reversal in permanent sleeper displacement is explained by frost heave. Further, based on inSAR data, the average landrise at the test site is in the order of 1–2 mm/year.

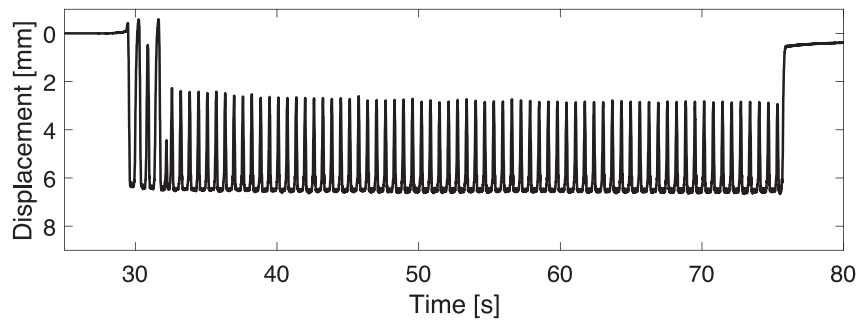To verify the reliability of the sleeper displacement measurements, a

Fig. 11. Example of low-pass filtered (30 Hz) displacement signal from sleeper 5 generated by a loaded iron ore train. Displacement is presented relative to the displacement before the first axle in the first locomotive. Measurement from 2022-12-07.
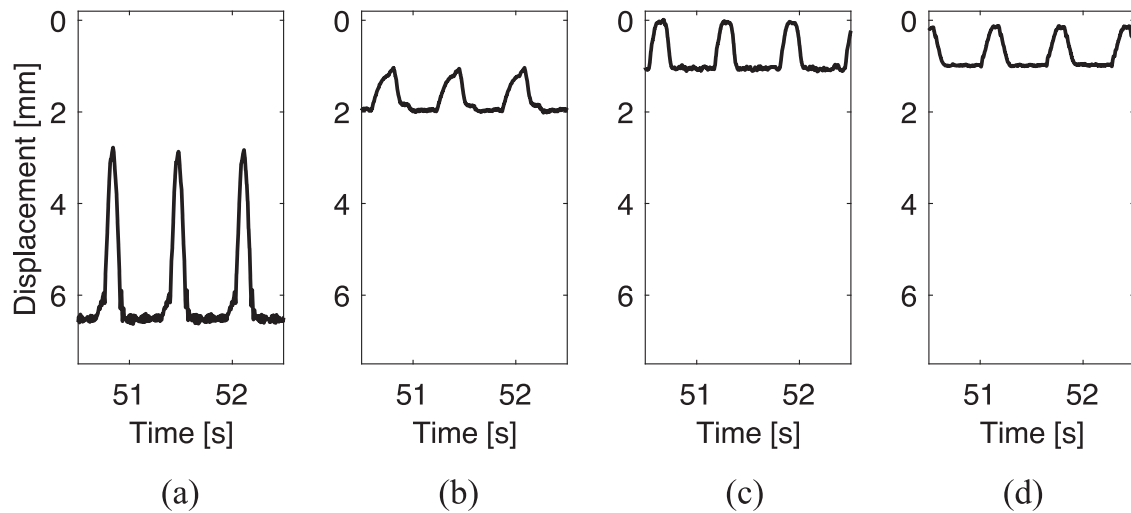

Fig. 12. Sleeper displacement generated by three pairs of adjacent bogies in a loaded iron ore train. (a) Sleeper 3, (b) sleeper 5, (c) sleeper 8, (d) sleeper 11. For each sleeper, the displacement is presented relative to the displacement before the first axle in the first locomotive, cf. Fig. 14. Positive sleeper displacement is downwards. Measurement from 2022-12-07.
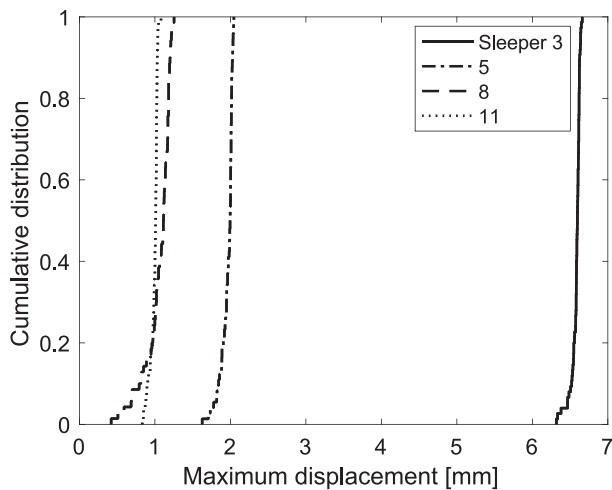

Fig. 13. Cumulative distribution of sleeper displacement along the transition zone due to the passing of one loaded iron ore train. Measurement from 2022-12-07.

comparison has been made with at rest track level measurements using a total station, see Fig. 15. The sleeper level survey was carried out using a Trimble SX12 self-levelling, automatic-scanning total station and an active prism. The prism was placed in line with markings on the sleeper

ends along the transition zone (sleepers 1 to 11), on sleepers 27 and 31 (to be used as reference points far from the transition), plus at two points on top of the slab. The total station had an angular accuracy of 1 mm. The survey was made on six occasions over a period of ten months: on October 10th before train speed was raised to nominal speed, and on October 14th after train speed had been raised to nominal speed. Afterwards, surveys were made on October 27th, November 30th, February 9th, and April 21st. The measured results are shown relative to the measured levels from October 10th. The data confirms that the settlements adjacent to the transition were very significant until 2022-11-30, although there was no local maximum (dip) in settlement as was indicated in the pre-test simulations [36]. This difference might be due to the large settlements of the 3MB slab track soon after it was built. Then, the degradation curves were reversed towards smaller settlements. This can be seen in both the displacement transducer data and the total station surveys between 2022-11-30 and 2023-04-21.

Overall, the long-term sleeper displacement data align well with the total station survey results for the ballasted track until the end of December. However, after that, due to the relative measurement of the FBG system with respect to a ground anchor, the upward movement of sleepers 3, 5, and 8 due to frost heave is not as significant and less than what the total station survey recorded. This occurs because the lengths of the anchors (2, 0.5, and 2 m) are shorter than the depth of the frozen ground. To achieve a fixed reference, longer anchors that reach below the frozen layers would have been needed. The total station survey agrees with the relative track displacement measurement in the case of sleeper 11, where the anchor length exceeds 4 m.
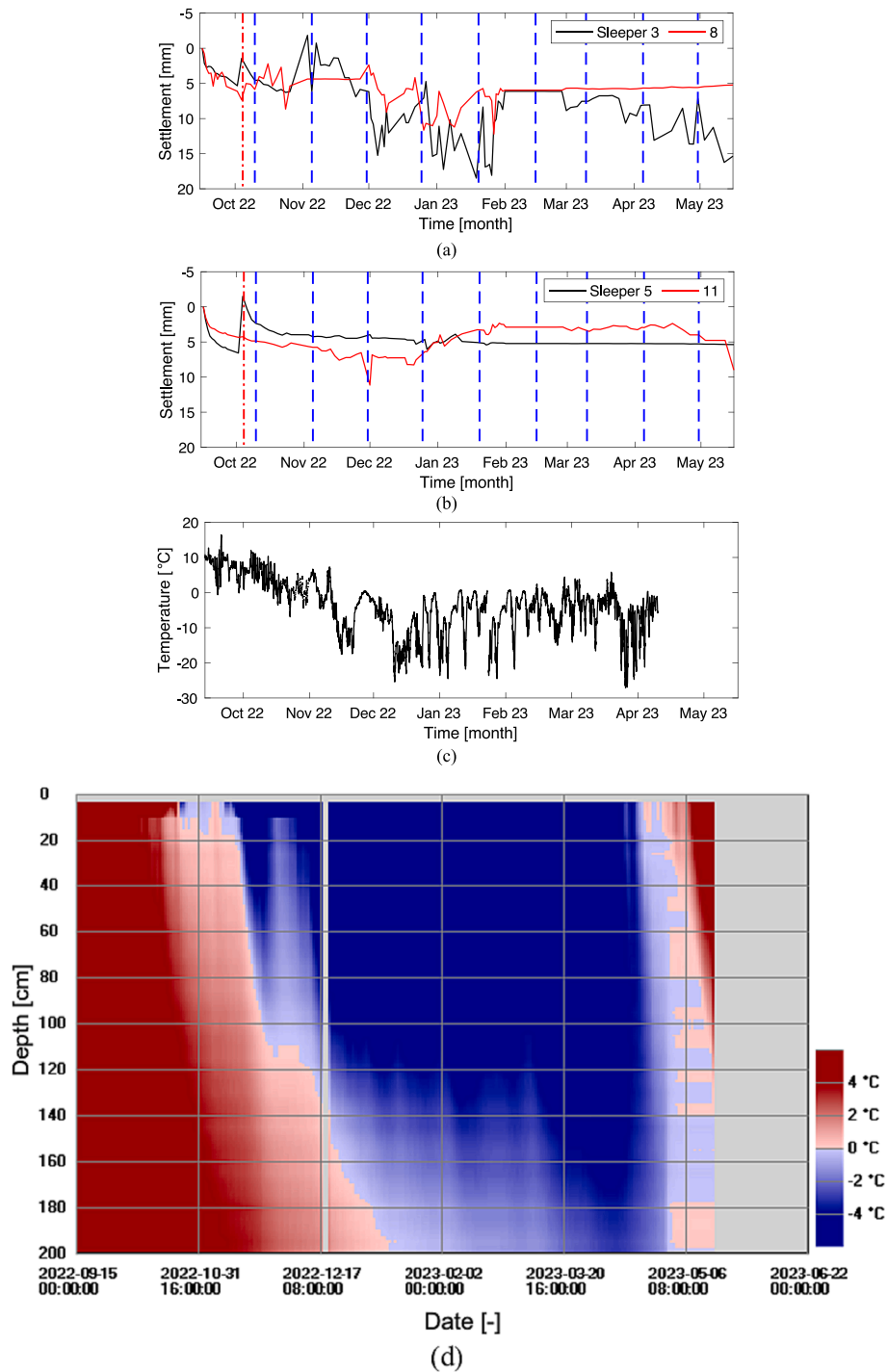
Fig. 14. (a) Evolution of unloaded sleeper displacement (settlement) over time for sleepers 3 and 8 (the displacement transducers were adjusted on site on 2022-10-04, 2022-10-25 and 2023-01-27), and (b) 5 and 11 (c) Ambient air temperature at the test site. (d) Temperature profile of subgrade up to 2 m depth at a measurement station near the test site. Copied from [46].

Complementary measurements

In addition to the discussed instrumentation of the transition zone, the wheel–rail contact force in selected sleeper bays was measured using the temporary electrical strain gauges described in Section 3.3. Contact forces were only monitored on two occasions, in October 2022 and May 2023, when visiting the test site with a separate logger.

Additionally, a track recording car was used for quality control of the longitudinal level of the track. The same car was used to measure the vertical track stiffness at rail level along the ballasted track, slab track

and transition zone with a sampling distance of 5 cm [38]. The stiffness measurements were carried out before construction of the 3MB slab track on June 5th, 2022, and after construction, on October 6th, 2023. It was based on this quality control that train speed could be raised to nominal speed on October 13th, 2022.

Wheel–rail contact force

An example of recorded strain signals in sleeper bays 3, 5 and 8 during the passing of one locomotive wheel are presented in Fig. 16(a).
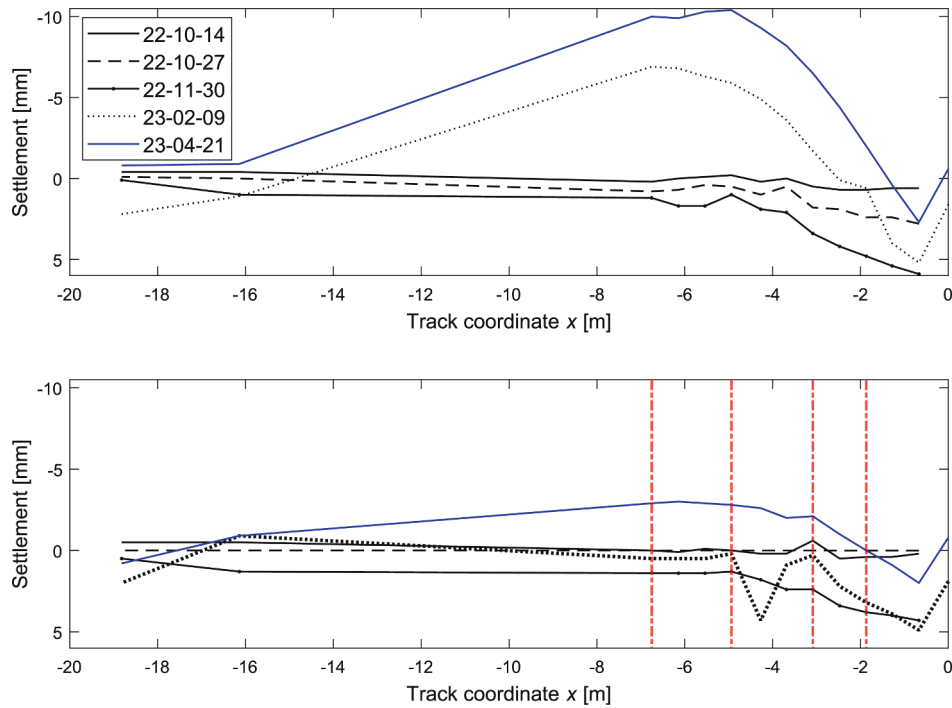
Fig. 15. Measured unloaded sleeper end settlement based on repeated total station surveys along 20 m of ballasted track (31 sleepers). Data is presented relative to the measurement on October 10th, 2022. (a) Field side of the track where the sensor clusters were installed, (b) track side. The data for position $x = 0$ m corresponds to the measurement position on the first block in the slab track, where track coordinate x is indicated in Fig. 3. The red vertical dashed lines show (from right) the positions of sleepers 3, 5, 8, and 11. (For interpretation of the references to colour in this figure legend, the reader is referred to the web version of this article.)
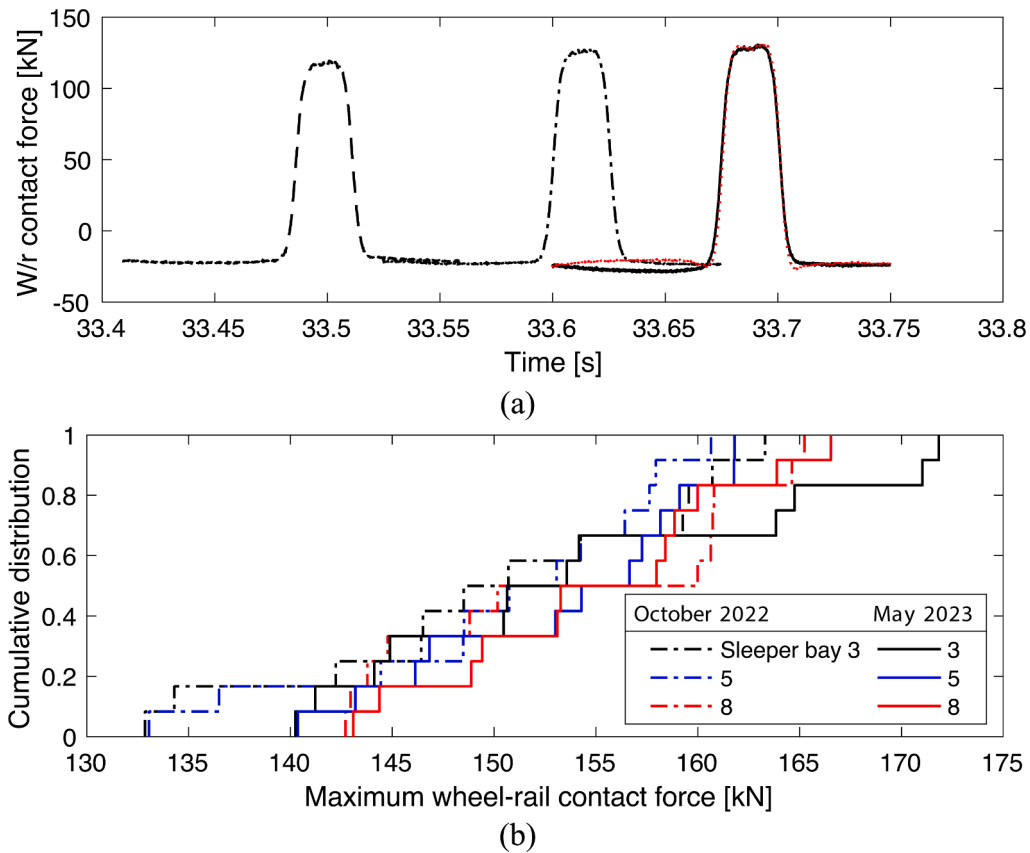

Fig. 16. (a) Vertical wheel-rail contact force measured at four positions in three sleeper bays. For each sleeper bay, the signal illustrates the passing of one loco-motive wheel. (b) Cumulative distributions of maximum wheel–rail contact forces for 12 locomotive wheels measured on two occasions. Measurements from 2022-10-25 and 2023-05-17.

The measured results from the instrumentation on the inner (track side) and outer (field side) parts of the rail in sleeper bay 3 are essentially overlapping. Thus, it can be concluded that any lateral offset in vertical loading or influence of lateral wheel–rail contact force is negligible in these measurements, and that measuring strain using (optical) strain gauges on only one side of the rail would have been sufficient in this transition zone. The relation (scaling factor) between shear strain measured at the neutral axis of the rail and a quasi-static wheel loading was determined based on the calibration field test with a slowly passing locomotive (5 km/h). In this study, the scaling factor 810 N/με was used to convert measured shear strain to wheel–rail contact force. Based on the maximum contact force generated by each of the axles in the two CoCo locomotives of one loaded iron ore train, the cumulative distribution functions of maximum contact force are presented in Fig. 16(b). It is observed that the wheel–rail contact force is higher in sleeper bay 3 than in sleeper bays 5 and 8, which is expected since the accumulated settlement at sleeper 3 was significant resulting in a voided sleeper. Based on the average of the maximum contact forces measured for all 12 locomotive wheels in sleeper bay 3, the wheels were generating in the order of 5 kN higher wheel–rail contact forces in May 2023 due to the evolving irregularities in longitudinal level along the transition.

Track stiffness

The measured track stiffness at rail level is presented in Fig. 17. A large gradient in stiffness is observed at either end of the 48 m slab track. The mean value of the track stiffness is particularly low for the slab track due to the softer elastic pads and the poor compaction of the back fill material after the excavation that was carried out during the construction. There are 11 local stiffness minima on the slab side that can be explained by the design of the track structure leading to a lower stiffness at each intersection between two modules (and also before the first module and after the last module). The stiffnesses at some distance away from the two transitions, measured before and after construction, are very similar indicating repeatability in the measurements.

Concluding remarks

A setup based on FBG sensors for in-situ long-term condition monitoring of track bed degradation in a transition zone between a conventional ballasted track and a 48 m field demonstrator section of a 3MB slab track has been developed and implemented. The measurements commenced in September 2022 and finished in June 2023. The system was designed for measurements in an operational railway track in harsh conditions (heavy haul traffic and low temperatures) at the test site Gransjö in the north of Sweden. The instrumentation along the transition comprised four clusters, each with an optical strain gauge array on the rail web in one sleeper bay, and an accelerometer and a

displacement transducer on the sleeper. Two additional accelerometers were installed on sleepers far from the transition zone to measure a reference state. A LabVIEW-based programme read, formatted, and stored the data locally. Subsequently, the data was synchronised with a server at Chalmers University of Technology. The ability for remote configuration of the system helped to adapt to the needs of the project.

It is unfortunate that the conditions for the construction of the transition zone at Gransjö were not optimal. As described in Section 2, during the excavation for the slab track, big blocks (boulders) were detected throughout the soil profile with a larger occurrence near the surface. Therefore, during the construction of the 3MB slab track, an extra excavation depth was required to remove those blocks. The excavated volume was replaced with not sufficiently compacted back fill material before construction of the slab, which led to significant settlement of the slab track soon after construction. Based on results presented in this paper, the settlement of the slab track continued although at a lower rate. This had a significant effect on the support conditions for the sleepers close to the transition, as particularly indicated by the measured short-term displacements and long-term settlement of sleeper 3. The construction of the transition zone was beyond control of the present study.

Nevertheless, it is concluded that the implemented sensors worked reliably and that the measurements were consistent. Using the FBG-based strain gauges, the setup was able to detect the type of vehicle, train speed, and number of axles passing over a sensor. The spatial and temporal resolution of the observed distribution of rail curvature was found to be sufficient for analysis of rail bending moment. A considerable variation in measured displacements between different sleepers in the transition zone was observed. These displacements depend on the virgin and evolving support conditions of each sleeper and its distance to the transition. For example, sleeper number 3 from the transition was voided soon after its installation due to substantial settlement, while sleeper 8 seems to have been supported by a very stiff foundation leading to low settlement. To verify the reliability of the displacement measurements, a comparison was made with at rest track level measurements using a total station. Good agreement between the measured degradation using the FBG sensors and the total station was observed. In general, the collected data can be used for the calibration of a model for simulation of dynamic vehicle–track interaction and long-term degradation of a transition zone. Further, it is argued that relevant parts of the demonstrated setup could be employed by infrastructure managers to justify, test, and evaluate new track designs across the network.

CRediT authorship contribution statement

Kourosh Nasrollahi: Conceptualization, Data curation, Formal analysis, Investigation, Methodology, Software, Validation, Writing – original draft. **Jelke Dijkstra:** Conceptualization, Methodology,
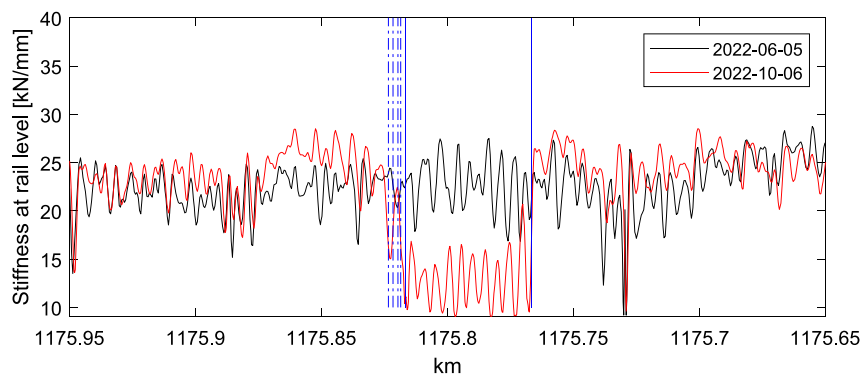

Fig. 17. Track stiffness of two transition zones and slab track at Gransjö measured by track recording car before and after construction. Blue vertical solid lines show the position of two transitions (slab ends). Blue vertical dashed-dotted lines show the positions of sleepers 3, 5, 8, and 11 numbered from the slab. (For interpretation of the references to colour in this figure legend, the reader is referred to the web version of this article.)

Resources, Supervision, Writing – review & editing. **Jens C.O. Nielsen:** Conceptualization, Funding acquisition, Methodology, Project administration, Resources, Supervision, Writing – review & editing.

References

[1] Indraratna B, Babar Sajjad M, Ngo T, Gomes Correia A, Kelly R. Improved performance of ballasted tracks at transition zones: A review of experimental and modelling approaches. Transp Geotech 2019;21:100260.

[2] Wang H, Markine V. Dynamic behaviour of the track in transition zones considering the differential settlement. J Sound Vib 2019;459:114863.

[3] Sañudo R, Jardí I, Martínez JC, Sánchez FJ, Miranda M, Alonso B, et al. Monitoring track transition zones in railways. Sensors 2022;22(1):76.

[4] Grossoni I, Hawksbee S, Jorge P, Bezin Y, Magalhaes H. Prediction of track settlement at high-speed railway transitions between embankment and bridge in the proximity of a turnout. Transp Geotech 2022;37:100879.

[5] Ramos A, Gomes Correia A, Calçada R, Connolly DP. Ballastless railway track transition zones: An embankment to tunnel analysis. Transp Geotech 2022:100728.

[6] Shan Y, Zhou S, Wang B, Ho CL. Differential settlement prediction of ballasted tracks in bridge–embankment transition zones. J Geotech Geoenviron Eng 2020; 146:1–18.

[7] Aggestam E, Nielsen JCO. Multi-objective optimisation of transition zones between slab track and ballasted track using a genetic algorithm. J Sound Vib 2019;446: 91–112.

[8] Wang H, Markine V. Modelling of the long-term behaviour of transition zones: Prediction of track settlement. Eng Struct 2018;156:294–304.

[9] Paixão A. Transition zones in railway tracks: An experimental and numerical study on the structural behaviour. Porto, Portugal: Faculty of Engineering, University of Porto; 2014. PhD Thesis.

[10] Nicks JE. The bump at the end of the railway bridge. Texas, United States: Texas A&M University; 2009. PhD Thesis.

[11] AREMA, Manual for railway engineering. Unit I Lanham, Maryland; 2019.

[12] Nielsen JCO, Oscarsson J. Simulation of dynamic train - track interaction with state-dependent track properties. J Sound Vib 2004;275:515–32.

[13] Powrie W, Le Pen L. A Guide to track stiffness. University of Southampton Department of Civil & Environmental Engineering; 2016.

[14] Milne D, Harkness J, Le Pen L, Powrie W. The influence of variation in track level and support system stiffness over longer lengths of track for track performance and vehicle track interaction. Veh Syst Dyn 2021;59:245–68.

[15] Indraratna B, Nimbalkar S, Neville T. Performance assessment of reinforced ballasted rail track. Proc Inst Civ Eng Ground Improv 2014;167:24–34.

[16] Sysyn M, Nabochenko O, Kovalchuk V. Experimental investigation of the dynamic behavior of railway track with sleeper voids. Railw Eng Sci 2020;28:290–304.

[17] Wang H, Markine V, Liu X. Experimental analysis of railway track settlement in transition zones. Proc Inst Mech Eng F J Rail Rapid Transit 2018;232:1774–89.

[18] Sauni M. Application of track geometry deterioration modelling and data mining in railway asset management. Finland: Faculty of Built Environment, Tampere University; 2022. PhD Thesis.

[19] Sañudo R, Dell'Olio L, Casado JA, Carrascal IA, Diego S. Track transitions in railways: A review. Constr Build Mater 2016;112:140–57.

[20] Le Pen L, Milne D, Thompson D, Powrie W. Evaluating railway track support stiffness from trackside measurements in the absence of wheel load data. Can Geotech J 2016;53:1156–66.

[21] Milković D, Simić G, Jakovljević Ž, Tanasković J, Lučanin V. Wayside system for wheel-rail contact forces measurements. Measurement 2013;46:3308–18.

[22] Wheeler LN, Take WA, Hoult NA. Performance assessment of peat rail subgrade before and after mass stabilization. Can Geotech J 2017;54:674–89.

[23] Filograno ML, Rodríguez-Barrios A, González-Herraez M, Corredera P, Martín-López S, Rodríguez-Plaza M, et al. Real time monitoring of railway traffic using Fiber Bragg Grating sensors. Proceedings of the ASME Joint Rail Conference 2010, 2010;2:493–500.

[24] Murray CA, Take WA, Hoult NA. Measurement of vertical and longitudinal rail displacements using digital image correlation. Can Geotech J 2014;52:141–55.

[25] Wheeler LN, Pannese E, Hoult NA, Take WA, Le H. Measurement of distributed dynamic rail strains using a Rayleigh backscatter-based fiber optic sensor: Lab and field evaluation. Transp Geotech 2018;14:70–80.

[26] Wheeler LN, Take WA, Hoult NA, Le H. Use of fiber optic sensing to measure distributed rail strains and determine rail seat forces under a moving train. Can Geotech J 2019;56:1–13.

[27] Coelho B, Hölscher P, Priest J, Powrie W, Barends F. An assessment of transition zone performance. Proceedings of the Institution of Mechanical Engineers, Part F: Journal of Rail and Rapid Transit 2011;225:129–39.

[28] Mishra D, Tutumluer E, Boler H, Hyslip JR, Sussmann TR. Railroad track transitions with multidepth deflectometers and strain gauges. Transp Res Rec 2014;2448:105–14.

[29] Milne D, Le Pen L, Watson G, Thompson D, Powrie W, Hayward M, et al. Proving MEMS technologies for smarter railway infrastructure. Procedia Eng 2016;143: 1077–84.

[30] Li C, Tang J, Cheng C, Cai L, Yang M. FBG arrays for quasi-distributed sensing: A review. Photonic Sensors 2021;11:91–108.

[31] Kouroussis G, Kinet D, Moeyaert V, Dupuy J, Caucheteur C. Railway structure monitoring solutions using fibre Bragg grating sensors. International Journal of Rail Transportation 2016;4:135–50.

[32] Kouroussis G, Caucheteur C, Kinet D, Alexandrou G, Verlinden O, Moeyaert V. Review of trackside monitoring solutions: From strain gages to optical fibre sensors. Sensors 2015;15:20115–39.

[33] Lai CC, Kam JCP, Leung DCC, Lee TKY, Tam AYM, Ho SL, et al. Development of a fiber-optic sensing system for train vibration and train weight measurements in Hong Kong. Sensors 2012;2012:7.

[34] Milne D, Le Pen L, Thompson D, Powrie W. Properties of train load frequencies and their applications. J Sound Vib 2017;397:123–40.

[35] Wang P. Longitudinal force measurement in continuous welded rail with bi-directional FBG strain sensors. Smart Material and Structures 2015;25.

[36] Nasrollahi K, Nielsen JCO, Aggestam E, Dijkstra J, Ekh M. Prediction of long-term differential track settlement in a transition zone using an iterative approach. Eng Struct 2023.

[37] Morales-Gamiz FJ. Design requirements, concepts, and prototype test results for new system of ballastless system (3MB slab track). Capacity for rail; Deliverable 2017;11:3.

[38] Nielsen JCO, Berggren EG, Hammar A, Jansson F, Bolmsvik R. Degradation of railway track geometry – Correlation between track stiffness gradient and differential settlement. Proc Inst Mech Eng F J Rail Rapid Transit 2020;234: 108–19.

[39] Trafikverket. Markteknisk undersökningsrapport, Geoteknik och Miljögeoteknik, Gransjö, Boden, (Survey of ground conditions, in Swedish), Sweden, Report number: TRV2014/165 445; 2014.

[40] Park CB, Miller RD, Xia J. Multichannel analysis of surface waves. Geophysics 1999;64(3):800–8.

[41] Knappett J, Craig RFC. Soil Mechanics. 9th ed. CRC Press; 2019.

[42] Nasrollahi K, Dijkstra J, Nielsen JCO, Ekh M. Long-term monitoring of settlements below a transition zone in a railway structure. Proceedings of the 11th International Symposium on Field Monitoring in Geomechanics, ISFMG2022, September 4–7, 2022, London, United Kingdom.

[43] Powrie W, Le Pen L, Milne D, Watson G, Harkness J. Behaviour of under-track crossings on ballasted railways. Transp Geotech 2019;21:100258.

[44] Boore DM, Bommer JJ. Processing of strong-motion accelerograms: Needs, options and consequences. Soil Dyn Earthq Eng 2005;25:93–115.

[45] Milne D, Le Pen L , Thompson D, Powrie W. Automated processing of railway track deflection signals obtained from velocity and acceleration measurements. Proc Inst Mech Eng F J Rail Rapid Transit 2018;232:2097–110.

[46] Trafikverket (the Swedish Transport Administration), https://tjaldjup.trafikverket. se/#/, 2023 [accessed July 5, 2023].